Dendritic solidification and characterization of a succinonitrile–acetone alloy

2006 J. Phys.: Condens. Matter 18 7825

(http://iopscience.iop.org/0953-8984/18/32/026)

INSTITUTE OF PHYSICS PUBLISHING JOURNAL OF PHYSICS: CONDENSED MATTER

J. Phys.: Condens. Matter **18** (2006) 7825–7839 doi:10.1088/0953-8984/18/32/026

Dendritic solidification and characterization of a succinonitrile–acetone alloy

Erkan Üstün, Emin Çadırlı and Hasan Kaya[1]

Faculty of Arts and Sciences, Department of Physics, Niğde University, 51200, Niğde, Turkey

E-mail: hkaya@nigde.edu.tr

Received 12 May 2006, in final form 16 June 2006
Published 31 July 2006
Online at stacks.iop.org/JPhysCM/18/7825

Abstract
A succinonitrile (SCN)–3.6 wt% acetone (ACE) alloy was unidirectionally solidified with a constant temperature gradient $G = 5.7$ K mm^{-1} in the growth rate ranges $V = 6.5$–113 μm s^{-1} and a constant growth rate $V = 6.5$ μm s^{-1} in the temperature gradient ranges $G = 3.5$–5.7 K mm^{-1}. The primary dendrite arm spacings, secondary dendrite arm spacings, dendrite tip radius and mushy zone depth were measured as a function of growth rate and temperature gradient. Theoretical models for the dendrite arm spacing and tip radius have been compared with the experimental observations, and a comparison of our results with the current theoretical models and previous experimental results has also been made. The stability constant (σ) for this alloy system was measured and this result was compared with various similar organic transparent alloys.

(Some figures in this article are in colour only in the electronic version)

1. Introduction

Over the last 40 years, the formation of dendrite arms during solidification has been studied extensively, and several studies [1–5] of directional solidification under steady-state conditions have been applied to dendritic growth in alloy systems. Dendritic growth is the ubiquitous form of crystal growth encountered when metals, alloys and many other materials solidify under low thermal gradients, a situation which typically occurs in most industrial solidification processes [1]. A dendrite structure is characterized by its microstructure parameters. Numerous solidification studies have been reported with a view to characterizing primary dendrite arm spacing (λ_1), secondary dendrite arm spacing (λ_2), dendrite tip radius (R) and mush zone depth (d) as a function of growth rate (V) and temperature gradient (G) ahead of the microscopic solidification front [5–19]. The effect of growth rate (V) on the primary dendrite spacing (λ_1), dendrite tip radius (R) and mushy zone depth (d) in various directionally solidified alloys was investigated in [15–19].

[1] Author to whom any correspondence should be addressed.

Recent empirical [6–9] and theoretical [10–12] studies have claimed the existence of an allowable range of stable spacings. This has been interpreted in such a way that no unique spacing selection criterion operates for λ, and an array with a band of spacings is stable under given experimental conditions. A literature survey shows several theoretical studies [5, 11, 20–31] and theoretical models [23, 26] and [32–37] used to examine the influence of solidification parameters (G, V) on microstructure parameters (λ_1, λ_2, R and d). The majority of results in the literature show a decrease in microstructure parameters with increasing V and G.

The goal of the present work was to experimentally investigate the dependency of λ_1, λ_2, R and d on V and $\mathbf{G}$ in a directionally solidified succinonitrile (SCN)–3.6 wt% acetone (ACE) binary transparent system and to compare the results with the current theoretical models [23, 26, 32–39] and previous experimental results [6, 15–17, 40–56].

1.1. Primary dendrite arm spacings

Hunt [32] and Kurz and Fisher [33] have proposed theoretical models to characterize cell/primary dendrite spacings (λ_1) as a function of growth rate (V), temperature gradients (G) and alloy composition (C_o) during steady-state growth conditions. Under the high velocity regime, the results predicted by these two theories differ only by a constant. The equations representing these two theories can be expressed, respectively, as:

$$\lambda_1 = 2.83[m(k-1)D\Gamma]^{0.25} C_o^{0.25} V^{-0.25} G^{-0.5} \qquad \text{(Hunt model)} \tag{1}$$

$$\lambda_1 = 4.3[m(k-1)D\Gamma/k^2]^{0.25} C_o^{0.25} V^{-0.25} G^{-0.5} \qquad \text{(Kurz and Fisher model)} \tag{2}$$

where Γ is the Gibbs–Thomson coefficient, m is the liquidus line slope, k is the solute partition coefficient and D is the liquid solute diffusivity.

Trivedi [34] has modified the Hunt model to characterize the dendritic primary spacing λ_1 as a function of G, V and C_o which can be expressed as

$$\lambda_1 = 2.83[m(k-1)D\Gamma L]^{0.25} C_o^{0.25} V^{-0.25} G^{-0.5} \qquad \text{(Trivedi model)} \tag{3}$$

where L is a constant depending on the harmonic of perturbation. Hunt and Lu [23] have proposed a numerical model to characterize the dendritic primary spacing λ_1. The model describes the steady state or unsteady state of an *axial* symmetric cell or dendrite and it can be expressed as

$$\lambda' = 0.077\,98 V'^{(a-0.75)} (V' - G')^{0.75} G'^{-0.6028} \qquad \text{(Hunt and Lu model)} \tag{4}$$

where $\lambda' = \lambda \Delta T_o/(\Gamma k)$, $G' = G\Gamma k/(\Delta T_o)^2$, $V' = V\Gamma k/(D\Delta T_o)$, $\Delta T_o = mC_o(k-1)/k$ and $a = -1.131$–$0.1555 \log G' - 0.007\,589(\log G')^2$.

Bouchard and Kirkaldy [35, 36] have also proposed a numerical model to characterize the dendritic primary spacing (λ_1) for unsteady-and steady-state heat flow conditions. A heuristically derived steady-state formula, after modification, is recommended by these authors for the purposes of predicting primary dendritic spacing in the unsteady regime and is given by:

$$\lambda_1 = a_1 \left(\frac{16 C_o^{1/2} G_o \varepsilon \Gamma D}{(1-k) m G V} \right)^{1/2} \qquad \text{(Bouchard and Kirkaldy model)} \tag{5}$$

where $G_o\varepsilon$ is a characteristic parameter (600×6 K cm^{-1}) and a_1 is the primary dendrite-calibrating factor [36].

1.2. Secondary dendrite arm spacings

Langer and Müller-Krumbhaar [26] have carried out a detailed numerical analysis of the wavelength of instabilities along the sides of a dendrite and have predicted scaling law as $\lambda_2/R = 2$. Using the scaling law $\lambda_2/R = 2$, the variation in λ_2 for small Peclet number conditions is given by Trivedi and Somboonsuk [37] as

$$\lambda_2 = (8\Gamma DL/kV\delta T_o)^{0.5} \qquad \text{(Trivedi and Somboonsuk model).} \tag{6}$$

For secondary dendrite arm spacings, Bouchard and Kirkaldy [36] derived an expression which is very similar that of to Mullins and Sekerka [38, 39]. This expression is independent of temperature gradient and is given by

$$\lambda_2 = 2\pi a_2 \left(\frac{4\Gamma}{C_o(1-k)^2 T_F} \left(\frac{D}{V} \right)^2 \right)^{1/3} \qquad \text{(Bouchard and Kirkaldy model)} \tag{7}$$

where a_2 is the secondary dendrite-calibrating factor, which depends on alloy composition, and T_F is the fusion temperature of the solvent. The Bouchard and Kirkaldy model depends additionally on empirical dimensionless calibration parameters a_1 for λ_1 and a_2 for λ_2, as shown by equations (5) and (7). These authors have proposed different a_1 values for different alloys [36, 43].

1.3. Dendrite tip radius

As mentioned in the previous section, the Hunt model [32], the Kurz–Fisher model [33] and the Trivedi model [34] have been applied to find the relationship between R as a function of V and C_o. According to the Hunt model [32],

$$R = [2\Gamma D/m(k-1)]^{0.5} C_o^{-0.5} V^{-0.5}, \tag{8}$$

according to the Kurz–Fisher model [33],

$$R = 2\pi[\Gamma D/m(k-1)]^{0.5} C_o^{-0.5} V^{-0.5} \tag{9}$$

and according to the Trivedi model [34],

$$R = [2k\Gamma DL/m(k-1)]^{0.5} C_o^{-0.5} V^{-0.5}. \tag{10}$$

As can be seen from equations (8)–(10) the theoretical models for dendritic tip radius, R, are also very similar and the difference between them is a constant only.

1.4. Approaches for mushy zone depth

Mushy zone depth d is described as the distance between a dendrite tip and its root. For binary alloy systems [57, 58] which cool without convection by using the constitutional undercooling criterion, d is given as

$$d \cong m(C_E - C_O)/G \tag{11}$$

(the phase diagram can be seen in [19, 59]) when $C_o > C_{SE}$ and $C_L = C_E$; the temperature required to return to this composition is the solidus temperature T_s and the temperature to return to C_t ($C_t \cong C_o$) is the liquidus temperature T_L. So, it is accepted that d is proportional to difference between T_L and T_S. The undercooling, ΔT_o is written as

$$\Delta T_o = -m\Delta C_o = T_L - T_S \tag{12}$$

by using equations (11) and (12) the mushy zone depth d can be written as follows

$$d = \frac{\Delta T_o}{G}. \tag{13}$$

1.5. Selection of the stability constant

Langer and Müller-Krumbhaar [26] have found dendrite tip radius as a function of some system parameters by using marginal stability criterion. The relationship is given by:

$$R = \left[\frac{I_{\mathrm{D}} d_o}{2\sigma^*}\right]^{1/2} \tag{14}$$

where σ^* is the stability constant, d_{o} is the capillarity length and I_{D} is the solute diffusion length, equal to

$$I_{\mathrm{D}} = \frac{2D}{V}. \tag{15}$$

The solute capillary length is given as

$$d_{\mathrm{o}} = \frac{\gamma}{\Delta S k \Delta T_{\mathrm{o}}} \tag{16}$$

where ΔT_{o} is the constitutional undercooling temperature ($\Delta T_{\mathrm{o}} = \frac{mc_O(1-k)}{k}$), ΔS is the effective entropy change of melting per unit volume and Γ is the Gibbs–Thomson coefficient ($\Gamma = \frac{\gamma}{\Delta S}$) [62]. If ΔT_{o} and Γ are substituted in equation (16) it can be written as follows [60, 61]:

$$d_{\mathrm{o}} = \frac{\Gamma}{mc_O(1-k)}. \tag{17}$$

If equation (14) is rearranged, the stability constant can be written as follows [60, 63]:

$$\sigma^* = \frac{D\Gamma}{VR^2 mc_O(1-k)}. \tag{18}$$

The physical meaning of the stability constant σ^* becomes apparent when considering a limiting case and the undercooling vanishes. In this case the radius of curvature of the dendrite becomes the radius of the tip curvature of a morphologically unstable sphere, R [64]. More generally, R is the initial radius of the perturbed unstable sphere that is determined by the particular experimental arrangement. For example, in Glicksman's experiments [1], a capillary was used to initiate the dendrite.

2. Experimental procedure

SCN–3.6 wt% ACE alloy was prepared from 99.9% pure SCN and 99.9% pure ACE supplied by the Sigma-Aldrich Chemical Company. The specimen was contained in a glass cell made from two glass cover slips (50 mm long, 24 mm wide and 0.05 mm thick). The slides were stuck together with a silicone elastomer. The slides were placed with their largest surface in the x–y plane and spaced a distance about 100–120 μm apart in the z direction to observe the dendrite in the x–y plane (2D). Organic materials usually react with this type of glue. Before filling the cell with alloy, the cell was annealed at 523 K to prevent reaction with the glue.

After filling the cell with alloy, the specimen cell was placed in the temperature gradient stage. Details of the experimental system were given in [15]. When one side of the cell was heated, the other side of the cell was kept cool with a water cooling system. The temperature of the heater was controlled to be ± 0.1 K with a *Eurotherm 905S* type controller. The temperatures in the specimen were measured with four insulated K type thermocouples 50 μm thick which were placed perpendicular to heat flow on the sample. The temperature gradient in front of the solid–liquid interface on the specimen during the solidification was observed to be constant.

The SCN–3.6 wt% ACE alloy was solidified in a horizontal directional solidification apparatus to directly observe the microstructures *in situ* using a transmission optical microscope. The solidification of the SCN–3.6 wt% ACE alloy was carried out with a constant temperature gradient ($G = 5.7$ K mm^{-1}) at five different growth rates ($V = 6.5$–113 μm s^{-1}) and a constant growth rate ($V = 6.5$ μm s^{-1}) at different temperature gradients ($G =$ 3.5–5.7 K mm^{-1}).

During the solidification, photographs of the microstructures were taken with an Olympus camera placed on a transmission Olympus BH2 optical microscope by using $\times 5$, $\times 10$, and $\times 20$ objectives and the photographs of a graticule ($100 \times 0.01 = 1$ mm) were also taken with same objectives.

2.1. Measurements of temperature gradient and growth rate

The specimen was slowly melted until the solid–liquid interface passed through the second thermocouple by driving the specimen cell toward the heating system. When the solid–liquid interface was between the second and third thermocouple, the synchronous motor was stopped and the specimen was left to reach thermal equilibrium. After the specimen reached a steady state, the solidification was started by driving the specimen toward the cooling system using a synchronous motor [16, 17].

When the interface passed the distance between two thermocouples the solidification time, Δt, and temperatures difference between two thermocouples, ΔT, were recorded simultaneously with a stopwatch and a Hewlett-Packard 34401-A multimeter, respectively. The thermocouple positions and solidification microstructures were photographed with an Olympus camera placed on an Olympus BH2 light optical microscope. Thus the distance between the two thermocouples, Δx, was measured accurately. The temperature gradient, $G = (\Delta T/\Delta x)$, and the growth rate, $V = (\Delta x/\Delta t)$, were determined by using the values of Δt, ΔT and Δx.

2.2. Measurements of primary dendrite arm spacings, secondary dendrite arm spacings, dendrite tip radius and mushy zone depth

The primary dendrite arm spacings (λ_1) were obtained by measuring the distances between the two nearest dendrite tips. The measurements of $\lambda_{1\ \mathrm{min}}$ (minimum), $\lambda_{1\ \mathrm{max}}$ (maximum) and $\lambda_{1\ \mathrm{average}}$ (average) were made for five different growth rates in a constant temperature gradient and five different temperature gradients a constant growth rate.

The relationship between $\lambda_{1\ \mathrm{min}}$, $\lambda_{1\ \mathrm{max}}$ and $\lambda_{1\ \mathrm{average}}$ for steady growth were obtained to be $\lambda_{1\ \mathrm{min}} < \lambda_{1\ \mathrm{average}} < \lambda_{1\ \mathrm{max}}$ and $\lambda_{1\ \mathrm{max}} \geqslant 2\lambda_{1\ \mathrm{min}}$. The secondary dendrite arm spacings (λ_2) were measured by averaging the distance between adjacent side branches of a primary dendrite as a function of the distance from the dendrite tip. The dendrite tip radius (R) was measured by fitting a suitable circle to the side of the dendrite tip. The mushy zone depth d is defined as the average distance between the tip and root of the dendrites.

In the measurements of λ_1, λ_2, R and d, 70–75 values of λ_1, λ_2, R and d for each growth rate and temperature gradient were measured to increase statistical sensitivity. Thus the values of λ_1, λ_2, R and d as a function of V and G for SCN–3.6 wt% ACE system were measured.

3. Results and discussion

The SCN–3.6 wt% ACE system alloy was solidified with a constant G at five different growth rates and a constant growth rate at five temperature gradients in order to experimentally

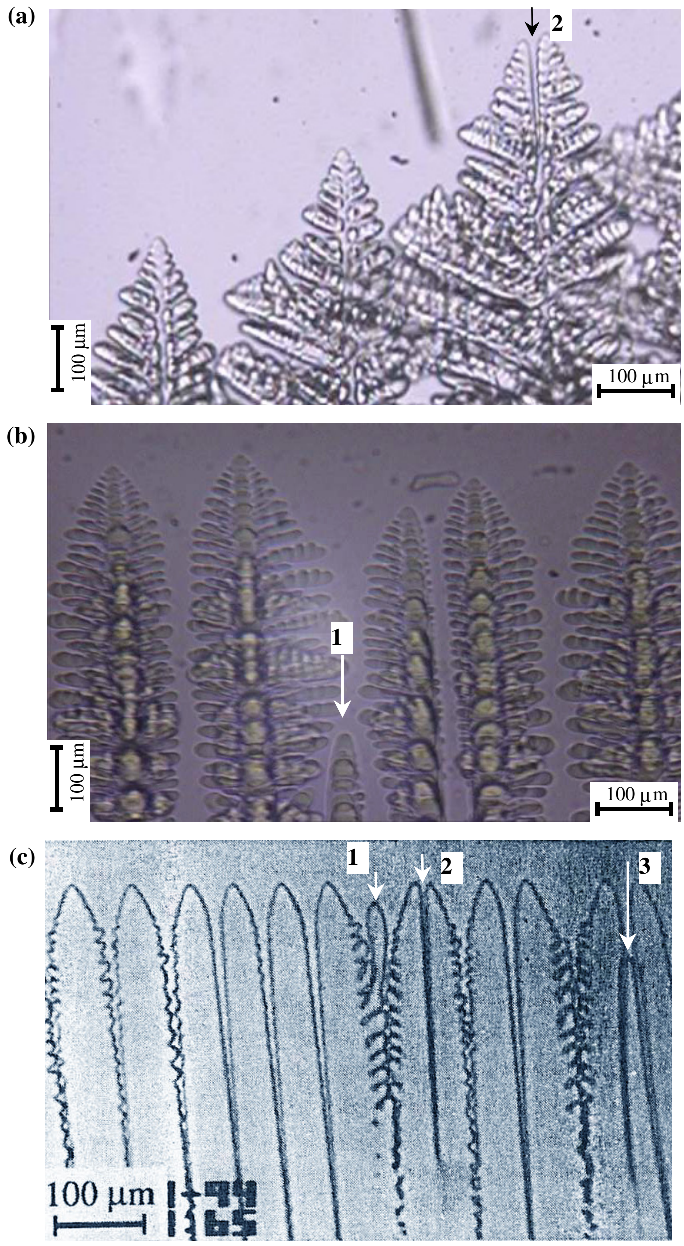

Figure 1. (a) Dendrite tip splitting (this work). (b) Dendrite elimination (this work). (c) All mechanisms: (1) growth of tertiary arm, (2) dendrite tip splitting, (3) dendrite elimination [61].

investigate the dependency of λ_1, λ_2, R and d on V and G, and to find the relationship between them.

The spacing between dendrites which show orientated growth during the solidification process varies: some of the spacing is narrow and some of the spacing is wide. The reason for this is dendrite elimination, dendrite tip splitting and the growth of tertiary arms. These mechanisms are shown in figure 1 [61]. To take these mechanisms into account, microstructure

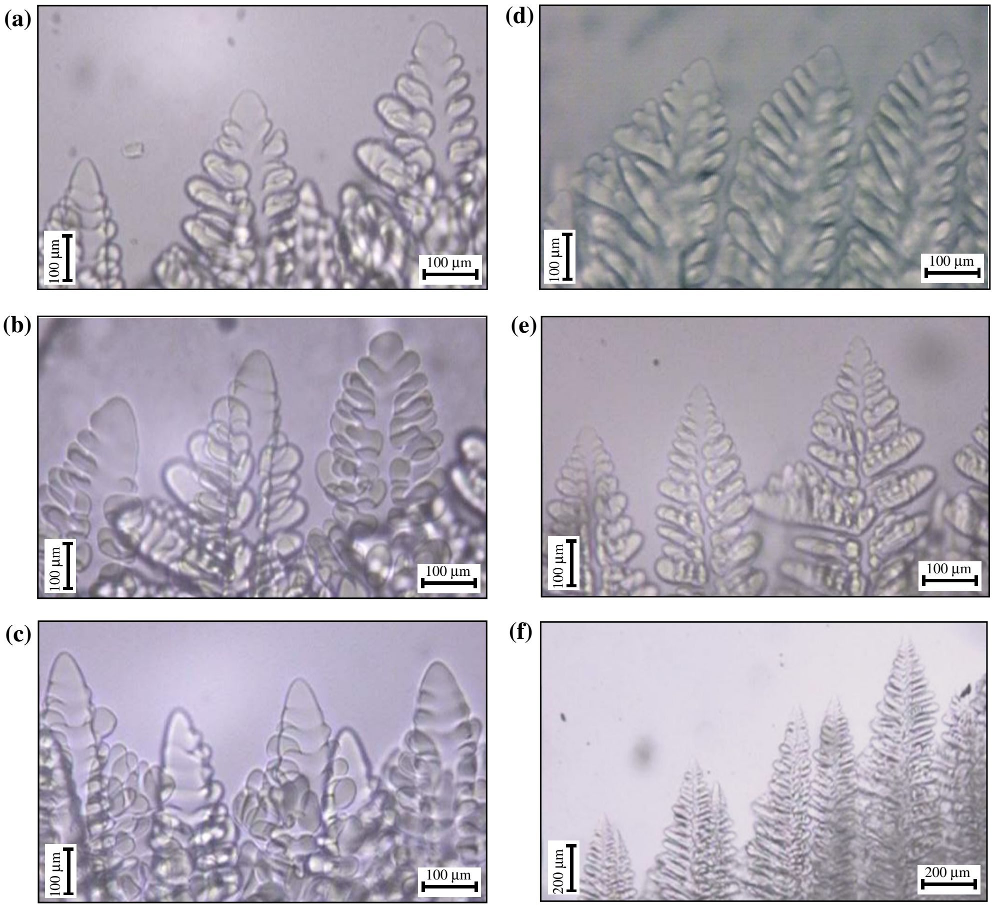

Figure 2. Solidification microstructures of SCN–3.6 wt% ACE alloy for constant V (6.5 μm s^{-1}): (a) $G = 3.53$ K mm^{-1}, (b) $G = 4.60$ K mm^{-1}, (c) 5.70 K mm^{-1} and for constant G (5.7 K mm^{-1}): (d) $V = 6.5$ μm s^{-1}, (e) $V = 34.2$ μm s^{-1}, (f) $V = 113$ μm s^{-1}.

parameters were measured from approximately 75 digital photographs for each growth rate and temperature gradient.

Typical microstructures of this alloy are shown in figure 2. The dependency of λ_1, λ_2, R and d on V and G was obtained by linear regression analysis and the results are given in tables 1 and 2. Figures 3(a)–(d) present the experimental values of λ_1, λ_2, R and d as a function of V and G, respectively.

As can be seen from figure 3(a), the values of λ_1, λ_2, R and d decrease as the temperature gradient increases at a constant V and the average exponent values of λ_1, λ_2, R and d in the directionally solidified SCN–3.6 wt% ACE alloy with a constant V at different temperature gradients were found to be −0.50, −0.50, −0.50 and −0.49, respectively. In figure 3(b) and table 1, the values of λ_1, λ_2, R and d decrease as the growth rate (V) increases at a constant G and the average exponent values of λ_1, λ_2, R and d in the directionally solidified SCN–3.6 wt% ACE alloy with a constant G at different growth rates were found to be −0.25, −0.48, −0.50 and −0.25, respectively.

A number of experimental studies have been reported in the literature to characterize the variations in λ_1, λ_2, R and d as a function of V, G [15]. The exponent values of λ_1, λ_2, R and

Table 1. Experimental relationships for the directionally solidified SCN–3.6 wt% ACE alloy.

Experimental relationships (constant V)		
$\lambda_{1\,(max)} = k_1 G^{-0.50}$	$k_1 = 13.2\ (\mu m^{0.5}\ K^{0.5})$	$r_1 = -0.995$
$\lambda_{1\,(ave)} = k_2 G^{-0.50}$	$k_2 = 9.7\ (\mu m^{0.51}\ K^{0.49})$	$r_2 = -0.996$
$\lambda_{1\,(min)} = k_3 G^{-0.49}$	$k_3 = 11.1\ (\mu m^{0.5}\ K^{0.5})$	$r_3 = -0.991$
$\lambda_2 = k_4 G^{-0.50}$	$k_4 = 1.4\ (\mu m^{0.5}\ K^{0.5})$	$r_4 = -0.995$
$R = k_5 G^{-0.50}$	$k_5 = 0.5\ (\mu m^{0.5}\ K^{0.5})$	$r_5 = -0.998$
$d = k_6 G^{-0.49}$	$k_6 = 18.4\ (\mu m^{0.51}\ K^{0.49})$	$r_6 = -0.992$
$\lambda_2 / R_{ave} = 2.6$		
Experimental relationships (constant G)		
$\lambda_{1\,(max)} = k_7 V^{-0.25}$	$k_7 = 280.9\ (\mu m^{1.25}\ sn^{-0.25})$	$r_7 = -0.987$
$\lambda_{1\,(ave)} = k_8 V^{-0.25}$	$k_8 = 240.1\ (\mu m^{1.25}\ sn^{-0.25})$	$r_8 = -0.990$
$\lambda_{1\,(min)} = k_9 V^{-0.25}$	$k_9 = 199.3\ (\mu m^{1.25}\ sn^{-0.25})$	$r_9 = -0.994$
$\lambda_2 = k_{10} V^{-0.48}$	$k_{10} = 49.5\ (\mu m^{1.48}\ sn^{-0.48})$	$r_{10} = -0.962$
$R = k_{11} V^{-0.50}$	$k_{11} = 20.5\ (\mu m^{1.50}\ sn^{-0.50})$	$r_{11} = -0.958$
$d = k_{12} V^{-0.25}$	$k_{12} = 351.7\ (\mu m^{1.25}\ sn^{-0.25})$	$r_{12} = -0.984$
$\lambda_2 / R_{ave} = 2.6$		

Table 2. The values of the stability constant, σ^* (SCN, succinonitrile; CAMP, camphor; ETH, ethanol; PVA, pivalic acid).

Systems	σ^* values	Ref.
SCN–3.61 wt% ACE	0.018	This work
PVA	0.022	[47]
CBr_4–7.9 wt% C_2Cl_6	0.022	[55]
CBr_4–10.5 wt% C_2Cl_6	0.019	[55]
PVA–0.82 wt% ETH	0.055	[56]
SCN–5.5 mol% ACE	0.020	[70]
NH_4Cl–70 wt% H_2O	0.022	[71]
SCN	0.0195	[72]
CAMP	0.022	[73]
Cyclohexanol	0.027	[74]
NH_4Cl-H_2O	0.08	[75]
SCN-H_2O	0.0156	[76]

d for SCN–3.6 wt% ACE alloy obtained in the present work are in good agreement with the exponent values of λ_1, λ_2, R and d obtained in previous works [15–19, 51–56, 65, 66].

Comparisons of the experimentally obtained λ_1 values in the present work with the values of λ_1 calculated using the Hunt [32], Kurz–Fisher [33], Trivedi [34], Hunt–Lu [23] and Bouchard–Kirkaldy [35, 36] models are given in figures 4(a)–(c). The physical parameters of SCN–3.6 wt% ACE alloy used in calculations of λ_1, λ_2, R and d with the theoretical models are given in table A.1. As can be seen from figures 4(a) and (b), the calculated lines of λ_1 with the Kurz–Fisher [33], Hunt [32] and Trivedi [34] models are much higher, slightly higher and slightly lower, respectively, than our experimental values, and the calculated line of λ_1 with the Hunt–Lu [23] model is slightly higher than the experimental values at a low growth rate (especially growth rates ranging between 35 and 113 $\mu m\ s^{-1}$); but these values of λ_1 are discrepancies from the experimental values at the lower growth rates (especially for growth rates lower than 35 $\mu m\ s^{-1}$).

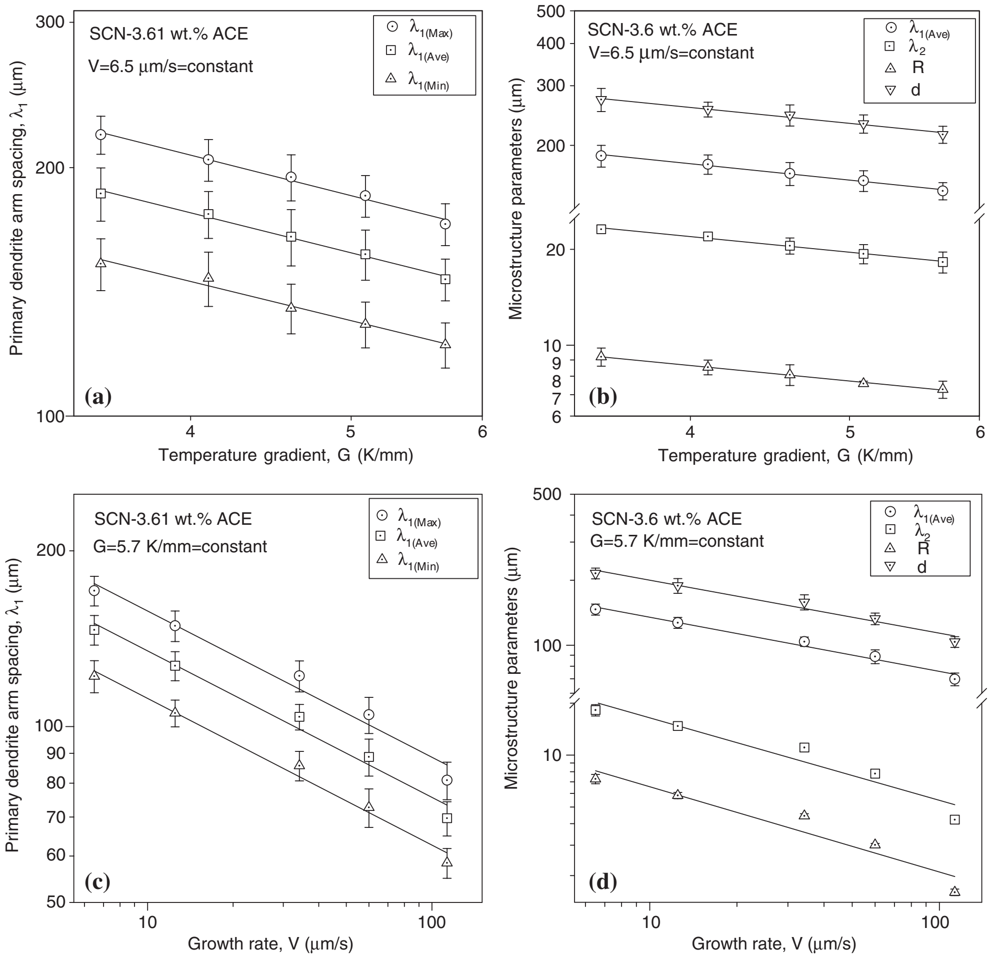

Figure 3. Variation of microstructure parameters according to solidification parameters: (a) variation of primary dendrite arm spacings as a function of G at a constant V; (b) variation of microstructure parameters as a function of G at a constant V; (c) variation of primary dendrite arm spacing as a function of V at a constant G; (d) variation of microstructure parameters as a function of V at a constant G.

It can be seen from figure 4(c) that the calculated values of λ_1 with the Bouchard–Kirkaldy [35] model are in good agreement with our experimental results for high growth rates (especially 35–113 μm s^{-1}) and are somewhat higher than the experimental values at low growth rates (especially for growth rates lower than 40 μm s^{-1}). It can be seen from figures 3(a)–(c) that the values of λ_1 obtained experimentally in the present work are in good agreement with the calculated values of λ_1 using the Trivedi [34] and Kurz–Fisher [33] models for SCN–3.6 wt% ACE alloy.

The values of λ_2 obtained experimentally in the present work as a function of growth rate have been compared with the values of λ_2 calculated with the Trivedi–Somboonsuk [37] and Bouchard–Kirkaldy [35, 36] models, and the comparisons are given in figures 5(a) and (b). As can be seen from figure 5(a), the calculated lines of λ_2 from the Trivedi–Somboonsuk model [37] as a function of $(C_o V)^{-0.5}$ are slightly lower than our experimental values and the

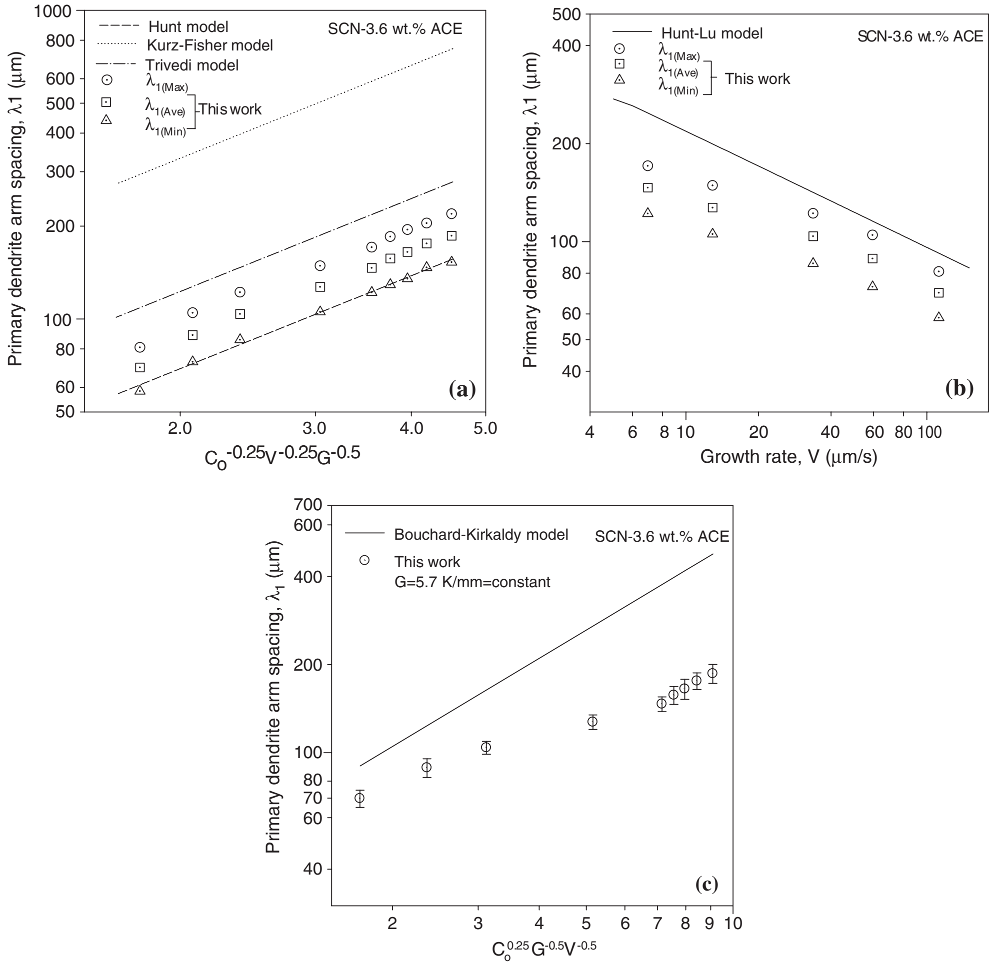

Figure 4. Comparison of experimental and theoretical λ_1 values as a function of V at a constant G for SCN–3.6 wt% ACE alloy.

calculated lines of λ_2 with the Bouchard–Kirkaldy model [35, 36] for SCN–3.6 wt% ACE alloy as a function of $C_o^{-0.33}V^{-0.67}$ are slightly higher than the our experimental values.

Figure 5(c) shows comparisons of the experimentally obtained R values as a function of $(C_oV)^{-0.5}$ in a constant temperature gradient with the values of R calculated from the Hunt [32], the Kurz–Fisher [33] and the Trivedi [34] models. It can be seen from figure 5(c) that the calculated lines of R with the Kurz–Fisher model [31] are in good agreement with our experimental values, the calculated lines of R with Trivedi model [34] are slightly lower than our experimental results and the calculated lines of R with the Hunt model [32] are much lower than our experimental values.

The variation of d with G is shown in figure 3(b). It can be seen that an increase in G produces a decrease in d. A regression analysis gives the proportionality equation as $d = k_6G^{-49}$. An increase in V also produces a decrease in d. As shown in figure 3(d) and table 1, d varies with V in the same manner as λ_1 varies with V. Thus, we can describe the relationship between d and V by a linear regression analysis as $d = k_{12}V^{-0.25}$.

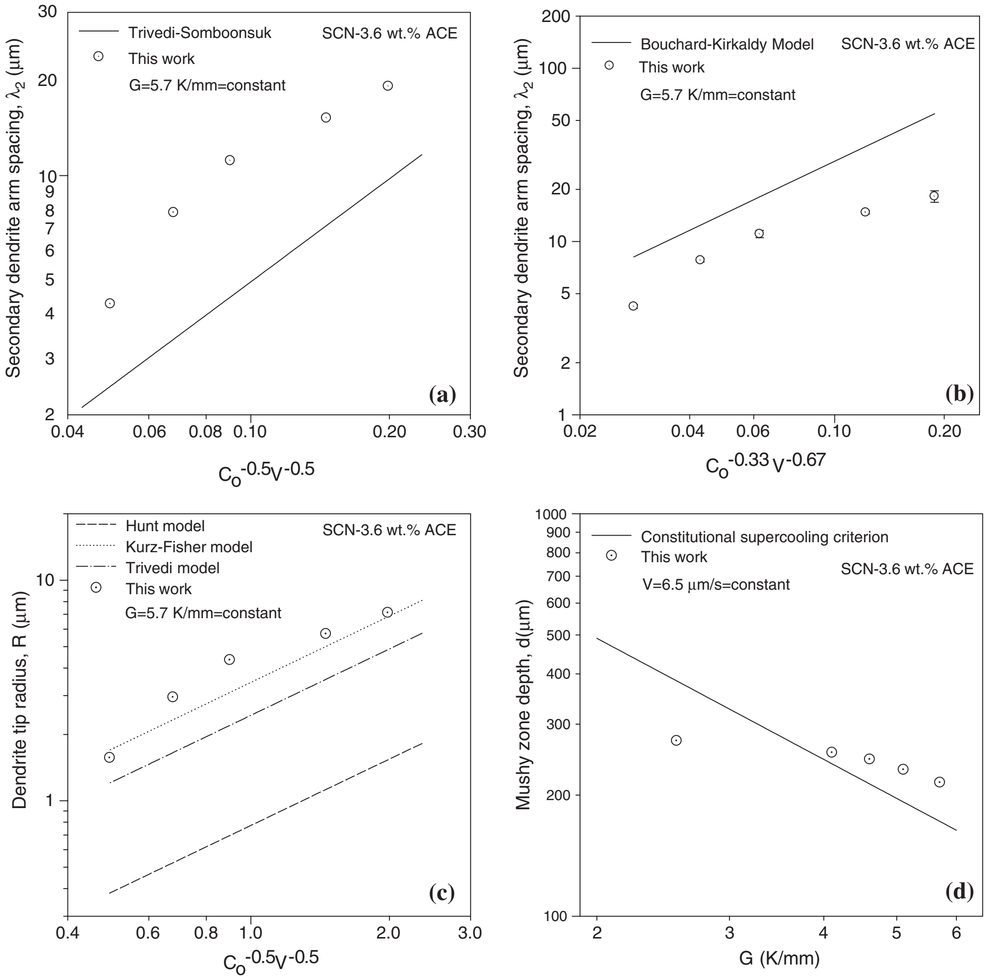

Figure 5. Comparison of experimental and theoretical values for (a) secondary dendrite arm spacing λ_2 as a function of $V^{-0.5}$, (b) secondary dendrite arm spacing λ_2 as a function of $V^{-0.67}$, (c) dendrite tip radius R as a function of $V^{-0.5}$ and (d) mushy zone depth d as a function of G for SCN–3.6 wt% ACE alloys.

A comparison of the experimentally obtained values for mushy zone depth d as an inverse function of G in the present work with the calculated d values using the Rutter–Chalmers [57, 58] model is given in figure 5(d) and the calculated line of d with the Rutter–Chalmers [57, 58] model is in good agreement at high experimental G (4.60–5.70) values.

The d values were found to be between 0.10 and 0.27 mm depending on G and V for SCN–3.6 wt% ACE organic alloy. The values of d in this work were slightly lower than the values (0.22–1.29 mm) measured by Çadırlı *et al* [15] for different succinonitrile–salol alloys. Also, the experimental d values were somewhat lower than the d values (38 mm), (7.7–28 mm) and (1.4–29.4 mm) obtained by Clyne [67], Tewari *et al* [68] and Gündüz and Çadırlı [19], respectively, for different metallic alloy systems.

The average value of λ_2/R for SCN–3.6 wt% ACE alloy is given in table 1 and the average value of λ_2/R is found to be 2.6. The values of λ_2/R for undercooled dendrites were estimated

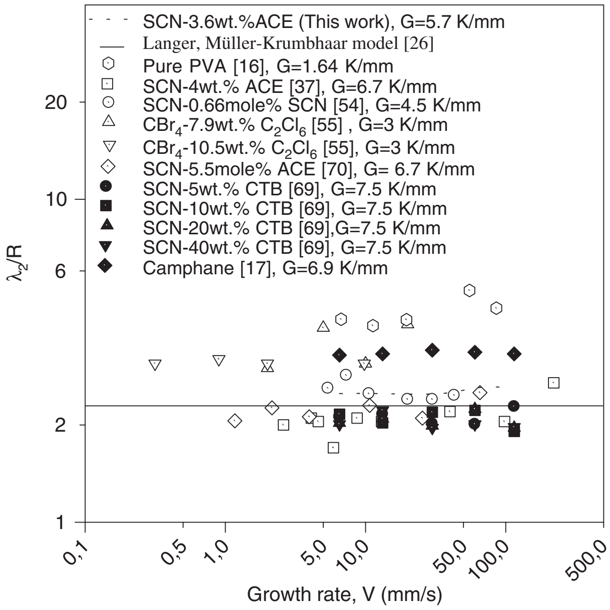

Figure 6. Comparison of λ_2/R values as a function of growth rate obtained in the present work with the theoretical and previous experimental works.

to be 2.1 by Langer and Müller-Krumbhaar [26]. As can be seen from figure 6, the average value of λ_2/R obtained in the present work for SCN–3.6 wt% ACE alloys is in good agreement with the value of λ_2/R estimated by Langer and Müller-Krumbhaar [26].

A comparison of λ_2/R values obtained in the present work with the previous experimental works [16, 17, 37, 54, 55, 69, 70] is also given in figure 6. The average value of λ_2/R for SCN–3.6 wt% ACE alloys obtained in the present work is in good agreement with the values of λ_2/R for different alloys obtained by previous workers.

The values of the stability constant σ^* calculated from equation (18) and calculated values in this work and available values in the literature are shown in table 2(b). The value of σ^* is in good agreement with the values of σ^* for different alloy systems obtained by previous workers [47, 55, 71–76]. The value of $\sigma^* = 0.018$ in this work is very close to the values of 0.022, 0.019, 0.022, 0.020 and 0.020 obtained by Glicksman and Singh [47], Seetharaman *et al* [55], Hansen *et al* [71], Huang and Glicksman [72] and Somboonsuk *et al* [73], respectively.

4. Conclusions

SCN–3.6 wt% ACE alloys were unidirectionally solidified with a constant V (6.5 μm s^{-1}) over a wide range of G (3.5–5.7 K mm^{-1}) and with a constant G (5.7 K mm^{-1}) over a wide range of V (6.5–113 μm s^{-1}). The microstructural features observed for the microstructural parameters (λ_1, λ_2, R, d) depend on the solidification parameters (G, V). The obtained results can be summarized as follows:

(1) Our experimental observations show that the values of λ_1, λ_2, R and d decrease as G and V increase. The relationship between the microstructure parameters (λ_1, λ_2, R and d) and the solidification parameters (G and V) with a constant solute composition have been obtained to be $\lambda_{1\,(\mathrm{ave})} = k_2 G^{-0.50}$, $\lambda_2 = k_4 G^{-0.50}$, $R = k_5 G^{-0.50}$, $d = k_6 G^{-0.49}$,

$\lambda_{1\,(\text{ave})} = k_8 V^{-0.25}$, $\lambda_2 = k_{10} V^{-0.48}$, $R = k_{11} V^{-0.50}$, $d = k_{12} V^{-0.25}$. These exponent values show that the dependency of λ_1 and d on G is stronger than on V, and also the dependences of λ_2, R on V are stronger than those of λ_1 and d.

(2) From the comparison, it can be seen that the average exponent values of λ_1, λ_2 and R are in good agreement with the corresponding theoretical exponent values.

(3) The values of λ_1, λ_2, R and d for directionally solidified SCN–3.6 wt% ACE alloys with a constant V and different G or with a constant G at different V measured in present work have been compared with the calculated values of λ_1, λ_2, R and d from the Kurz–Fisher [33], Trivedi [34], Bouchard–Kirkaldy [35, 36], Hunt–Lu [23], Trivedi–Somboonsuk [37] and Rutter–Chalmers [57, 58] models, and it was seen that the experimental results are mostly in good agreement with the calculated values from the these models.

(4) Langer and Müller-Krumbhaar [26] have predicted the values of λ_2/R to be 2.1. In the present work, the average value of λ_2/R for SCN–3.6 wt% ACE alloys was found to be 2.55.

(5) The value of the stability constant σ^* in this work is in good agreement with the values of σ^* for different alloys obtained by previous workers [47, 55, 70–76].

Appendix.

Table A.1. The physical constants for SCN–ACE alloy.

Liquidus slope (m)	3.02 (K/wt%) or 0.302 × 103 (K mol^{-1} fr^{-1})	[77]
Liquid diffusion coefficient (D)	12.7 × 10^2 μm^2 s^{-1}	[77]
Equilibrium partition coefficient (k)	0.1	[77]
The Gibbs–Thomson coefficient (Γ)	6.4 × 10^{-2} (K μm)	[77]
Equilibrium melting point of SCN (T_e)	330 K	[77]
The harmonic perturbations	10 mJ m^{-2}	[34]

References

[1] Glicksman M E and Koss M B 1994 Dendritic growth velocities in microgravity *Phys. Rev. Lett.* **73** 573–6

[2] Verheoven J D 1975 *The Fundamentals of Physical Metallurgy* (Canada: Wiley) p 3

[3] Koss M B, LaCombe J C, Tennenhouse L A, Glicksman M E and Winsa E A 1999 Dendritic growth tip velocities and radii of curvature in microgravity *Metall. Trans.* A **30** 3177

[4] Trivedi R and Kurz W 1994 Dendritic growth *Int. Mater. Rev.* **39** 49–74

[5] Mullins W W and Sekerka R F 1964 *J. Appl. Phys.* **35** 444–51

[6] Han S H and Trivedi R 1994 Primary spacing selection in directionally solidified alloys *Acta Metall.* **42** 25–41

[7] Pan Q Y, Huang W D, Lin X and Zhou Y H 1997 Primary spacing selection of Cu–Mn alloy under laser rapid solidification condition *J. Cryst. Growth* **181** 109–16

[8] Weidong H, Xingguo G and Yaohe Z 1993 Primary spacing selection of constrained dendritic growth *J. Cryst. Growth* **134** 105–15

[9] Ding G L, Huang W D, Huang X, Lin X and Zhou Y H 1996 On primary dendritic spacing during unidirectional solidification *Acta Metall.* **44** 3705–9

[10] Ding G L, Huang W, Lin X and Zhou Y 1997 Prediction of average spacing for constrained cellular/dendritic growth *J. Cryst. Growth* **177** 281–8

[11] Lu S Z and Hunt J D 1992 A numerical analysis of dendritic and cellular array growth: the spacing adjustment mechanisms *J. Cryst. Growth* **123** 17–34

[12] Warren J A and Langer J S 1993 Prediction of dendritic spacings in a directional-solidification experiment *Phys. Rev.* E **47** 2702–12

[13] Makkonen L 2000 Spacing in solidification of dendritic arrays *J. Cryst. Growth* **208** 772–8
[14] Walker D J and Mullis A M 2001 A mechanism for the equalisation of primary spacing during cellular and dendritic growth *J. Mater. Sci.* **36** 865–9
[15] Çadırlı E, Karaca I, Kaya H and Maraşlı N 2003 Effect of growth rate and composition on the primary spacing, the dendrite tip radius and mushy zone depth in the directionally solidified succinonitrile–salol alloys *J. Cryst. Growth* **255** 190–203
[16] Çadırlı E, Maraşlı N, Bayender B and Gündüz M 1999 Investigation of the structure parameters according to the solidification parameters for pivalic acid *J. Mater. Sci.* **34** 5533–41
[17] Çadırlı E, Maraşlı N, Bayender B and Gündüz M 2000 Dependency of the microstructure parameters on the solidification parameters for camphene *Mater. Res. Bull.* **35** 985–95
[18] Çadırlı E and Gündüz M 2000 The directional solidification of Pb–Sn alloys *J. Mater. Sci.* **35** 3837–48
[19] Gündüz M and Çadırlı E 2002 Directional solidification of aluminium–copper alloys *Mater. Sci. Eng.* A **327** 167–85
[20] Hunt J D 1990 A numerical analysis of time dependent isolated dendritic growth for conditions near the steady state *Acta Metall.* **38** 411–8
[21] Hunt J D 1991 A numerical analysis of dendritic and cellular growth of apure material investigating the transition from array to isolated growth *Acta Metall.* **39** 2117–33
[22] Hunt J D and Lu S-Z 1993 Numerical modelling of cellular and dendritic array growth: spacing and structure predictions *Mater. Sci. Eng.* A **173** 79–83
[23] Hunt J D and Lu S-Z 1996 Numerical modeling dendritic array growth: spacing and structure predictions *Metall. Trans.* A **27A** 611–23
[24] Burden M H and Hunt J D 1974 Cellular and dendritc growth II *J. Cryst. Growth* **22** 109–16
[25] Warren J A and Langer J S 1990 Stability of dendritic arrays *Phys. Rev.* A **42** 3518–25
[26] Langer J S and Müller-Krumbhaar H 1978 Theory of dendritic growth-I. Elements of a stability analysis *Acta Metall.* **26** 1681–7
[27] Laxmanan V 1985 Dendritic solidification-I. Analysis of current theories and models *Acta Metall.* **33** 1023–35
[28] Laxmanan V 1985 Dendritic solidification-II. A model for dendritic growth under an imposed thermal gradient *Acta Metall.* **33** 1037–49
[29] Paradies C J, Smith R N and Glicksman M E 1997 *Metall. Trans.* A **28** 875–83
[30] Farup I and Mo A 2000 Two-phase modeling of mushy zone parameters associated with hot tearing *Metall. Trans.* A **31** 1461–72
[31] Goyeau B, Benihaddadene T, Gobin D and Quintard M 1999 Numerical calculation of the permeability in a dendritic mushy zone *Metall. Trans.* B **30** 613–22
[32] Hunt J D 1979 *Solidification and Casting of Metals* (London: The Metal Society) p 3
[33] Kurz W and Fisher D J 1981 Dendritic growth and limit of stability tip radius and spacing *Acta Metall.* **29** 11–20
[34] Trivedi R 1984 Interdendritic spacing: part II. A. comparison of theory and experiment *Metall. Trans.* A **15A** 977–82
[35] Bouchard D and Kirkaldy J S 1996 Scaling of intragranular dendritic microstructure in ingot solidification *Metall. Mater. Trans.* B **27B** 101–13
[36] Bouchard D and Kirkaldy J S 1997 Prediction of dendrite arm spacings in unsteady- and steady-state heat flow of unidirectionally solidified binary alloys *Metall. Mater. Trans.* B **28** 651–63
[37] Trivedi R and Somboonsuk K 1984 Constrained dendritic growth and spacing *Mater. Sci. Eng.* **65** 65–74
[38] Sekarka R F 1965 A stability function for explicit evaluation of the Mullins-Sekerka interface stability criterion *J. Appl. Phys.* **36** 264–8
[39] Mullins W W and Sekarka R F 1965 Stability of a planar interface during solidification of a dilute binary alloy *J. Appl. Phys.* **35** 444–51
[40] Okamoto T and Kishitake K 1975 Dendritic structure in unidirectionally solidified aluminum, tin, and zinc base binary alloys *J. Cryst. Growth* **29** 137–46
[41] Sharp R M and Hellawell A 1969 The microscopy and composition of quenched solid–liquid interfaces *J. Cryst. Growth* **5** 155–61
[42] Spittle J A and LIoyd D M 1979 *Proc. Int. Conf. on Solidification and Casting of Metals* (London: The Metals Society) pp 15–20
[43] Quaresma J M V, Santos C A and Garcia A 2000 Correlation between unsteady-state solidification conditions, dendrite spacings, and mechanical properties of Al–Cu alloys *Metall. Mater. Trans.* A **31A** 3167–78
[44] Schaefer R J and Glicksman M E 1981 *Modeling of Casting and Welding Process* (Warendale, PA: TMS-AIME) p 55
[45] Jackson K A and Hunt J D 1965 Transparent compounds that freeze like metals *Acta Metall.* **13** 1212–5
[46] Glicksman M E 1971 *Solidification* (Ohio: American Society For Metals) p 155

[47] Glicksman M E and Sing N B 1986 *In Rapidly Solidified Powder Aluminum Alloys* ed M E Fine and E A Starke Jr (Philadelphia, PA: American Society for Testing and Materials) pp 44–61

[48] Schmidbauer W, Wilke T and Asmuss W 1993 In situ observation of growth morphologies in systems with high melting temperatures *J. Cryst. Growth* **128** 240–6

[49] De Cheveigne S, Guthman C and Lebrun M M 1985 Nature of transition of the solidification front of a binary mixture from a planar to a cellular morphology *J. Cryst. Growth* **73** 242–4

[50] Huang W, Geying X and Zhou Y 1993 Primary spacing selection of constrained dendritic growth *J. Cryst. Growth* **134** 105–15

[51] Taha M A 1979 Some observations on the dendritic morphology and dendrite arm spacings *Metall. Sci.* **1** 9–12

[52] Grugel R N and Zhou Y 1989 Primary dendrite spacing and the effect of off-axis heat flow *Metall. Trans.* A **20** 969–73

[53] Dey N and Sekhar J A 1993 Interface configurations during the directional growth of salol-I morphology *Acta Metall.* **41** 409–24

[54] Liu L X and Kirkaldy J S 1994 Systematic of thin film cellular-dendrites and the cell to dendrite transition in succinonitrile-salol, succinonitrile-acetone *J. Cryst. Growth* **140** 115–22

[55] Seetharaman V, Fabietti L M and Trivedi R 1989 Dendritic growth in the carbon tetra bromide and hexachlorethane system *Metall. Trans.* **20** 2567–70

[56] Trivedi R and Mason J T 1991 The effect of interface attachment kinetics on solidification interface morphologies *Metall. Trans.* A **22** 235–49

[57] Rutter J W and Chalmers B A 1953 Prismatic substructure formed during solidification of metals *Can. J. Phys.* **31** 15–39

[58] Tiller W A, Jackson K A, Rutter J W and Chalmers B 1953 The redistribution of solute atoms during the solidification of metals *Acta Metall.* **1** 428–37

[59] Kurz W and Fisher D J 1989 *Fundamentals of Solidification* (Aedermannsdorf, Switzerland: Trans Tech Publications) p 16

[60] Trivedi R and Somboonsuk K 1985 Pattern formation during the directional solidification of binary systems *Acta Metall.* **33** 1061–8

[61] Akamatsu S, Faivre G and Ihle T 1995 Symmetry-broken double fingers and seaweed patterns in thin-film directional solidification of a nonfaceted cubic crystal *Phys. Rev.* E **51** 4751–73

[62] Bayender B, Maraslı N, Çadırlı E, Şişman H and Gündüz M 1998 Solid–liquid surface energy of pivalic acid *J. Cryst. Growth* **194** 119–24

[63] Billia B and Trivedi R 1993 Pattern formation in crystal growth *Handbook of Crystal Growth* ed D T J Hurle (Amsterdam: Elsevier Science Publishers B.V.) pp 1026–46

[64] Pines V, Chait A and Zlatkowski M 1997 Dynamic scaling in dendritic growth: significance of the initial nucleus size *J. Cryst. Growth* **182** 219–26

[65] Esaka H and Kurz W 1985 Columnar dendrite growth: experiments on tip growth *J. Cryst. Growth* **72** 578–84

[66] Cattaneo C A, Evequoz O P and Bertorello H R 1994 Cellular and dendritic solidification in succinonitrile–water system *Scr. Metall.* **31** 461–6

[67] Clyne T W 1984 Modelling of heat flow in solidification *Mater. Sci. Eng.* **65** 111–24

[68] Tewari S N, Shah R and Song H 1994 Effect of magnetic field on the microstructure *Metall. Trans.* A **25** 1535–44

[69] Kaya H, Çadırlı E, Keşlioğlu K and Maraşlı N 2005 Dependency of the dendritic arm spacings and tip radius on the growth rate and composition in the directionally solidified succinonitrile–carbon tetrabromide alloys *J. Cryst. Growth* **276** 583–93

[70] Somboonsuk K, Mason J T and Trivedi R 1984 Interdendritic spacings; part 1: experimental studies *Metall. Trans.* A **15** 967–75

[71] Hansen G, Liu S, Lu S Z and Hellawell A 2002 Dendritic array growth in the systems NH_4ClH_2O and $[CH_2CN]_2$–H_2O: Steady state measurements and analysis *J. Cryst. Growth* **234** 731–9

[72] Huang S C and Glicksman M E 1981 Fundamentals of dendritic solidification-I. steady-state tip growth *Acta Metall.* **29** 717–34

[73] Rubinstein E R and Glicksman M E 1991 Dendritic growth kinetics and steucture I. Pivalic acid *J. Cryst. Growth* **112** 84–96

[74] Singh N B and Glicksman M E 1989 Free dendritic growth in viscous melts: cylohexanol *J. Cryst. Growth* **98** 534–40

[75] Dougherty A and Gollub J 1988 Steady-state dendritic growth of NH_4Br from solution *Phys. Rev.* A **38** 3043–6

[76] Maresca M J, Perez de Heluane S, Gervasoni J L and Bertorello H R 2003 Evaluation of the stability of free dendrites. Applications to water and succinonitrile *Int. J. Hydrog. Energy* **28** 69–75

[77] Gandin CH A, Eshelman M and Trivedi R 1996 Orientation dependence of primary dendrite spacing *Metall. Mater. Trans.* A **27** 2727–39